Proceedings of the
Annual Stability Conference
Structural Stability Research Council
Louisville, Kentucky, April 2-4, 2025

Buckling behavior of metal building under dynamic wind loads

Shihang Wang[1], Xinyang Wu[2], Delong Zuo[3], Hannah B. Blum[4]

Abstract
Metal building systems are cost-effective and versatile, and may serve as critical infrastructure, particularly in rural areas. While metal buildings are vulnerable to tornadoes, this is partly due to their large size, which increases the probability of being hit. Another reason is that their structural members are typically composed of slender elements, making them prone to buckling failure under high tornado wind speeds. Additionally, global buckling can be exacerbated by the strength or stiffness failure of compression flange bracing due to high bracing demands. To investigate the buckling resistance of metal buildings under tornado loading, this study first conducts laboratory testing using the tornado simulator at Texas Tech University to measure tornado loading on a metal building model. Then, a detailed full-scale finite element (FE) model of the metal building roof system was created in ABAQUS, included nonlinear material and geometric behavior, and standing seam roof details. The influence of the tornado wind pressure on the failure modes, including purlin buckling, is investigated. Furthermore, by applying different tornado loading scenarios, the finite element analysis can locate potential failure modes and critical members, offering a comprehensive assessment of the building's resiliency.

1. Introduction

Metal buildings are increasingly recognized as critical infrastructure that serves a wide range of applications such as industrial warehouses, agricultural storage facilities, commercial spaces, residences, and other public and private uses. Metal buildings are widely used because they are structurally efficient, easy to assemble, and adaptable to a variety of functional needs. However, it is important to ensure that these buildings serving critical needs remain functional after severe natural disasters such as tornadoes.

Tornadoes generate wind pressures that fluctuate at high speeds, creating complex non-linear stresses on structural components. Unlike static loads, these dynamic forces amplify instabilities such as buckling, a critical failure mode for thin-walled metal structures. Understanding and addressing the buckling behavior of metal buildings in such extreme conditions is critical to improving their resilience.

[1]Graduate Research Assistant, University of Wisconsin-Madison, <swang2378@wisc.edu>;
[2]Graduate Research Assistant, Texas Tech University , <xinyawu@ttu.edu>;
[3]Professor, Texas Tech University, <delong.zuo@ttu.edu>;
[4]Alain H. Peyrot Associate Professor, University of Wisconsin-Madison, <hannah.blum@wisc.edu>

In this paper, finite element analysis software ABAQUS (Abaqus, 2016) was used to create a high-fidelity 3D nonlinear model of the metal building using shell elements. The design drawings for the structure were provided by Chief Buildings. Fig.1a illustrates the design drawing, while Fig.1b presents the corresponding ABAQUS model. The structure is a 80 ft by 120 ft metal building system with a column height of 20 ft, consisting of both primary and secondary structural members. The roof has a slope of 1/2:12 pitch. Based on observations from the previous tornado damage report (Federal Emergency Management Agency (FEMA), 1999), roof panels were added to the model to account for diaphragm action and the effects of skin stresses (Rogers and Tremblay, 2010, Telue and Mahendran, 2004).

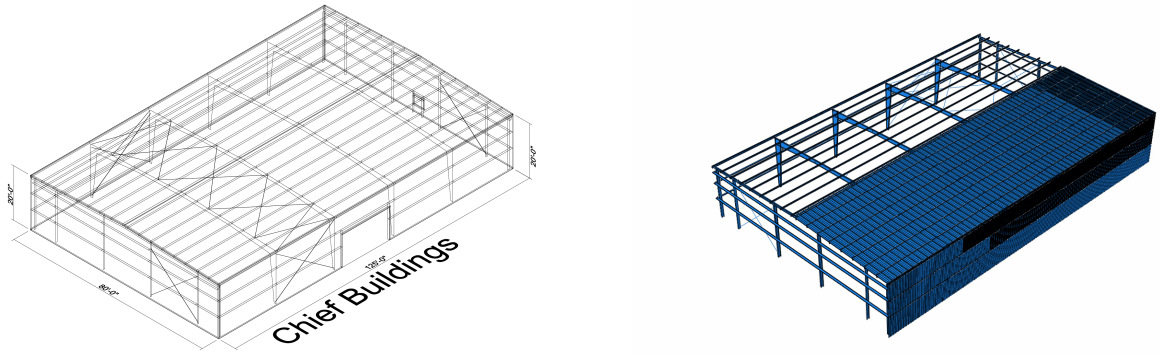

(a) Prototype provided by Chief Buildings

(b) Whole frame model in ABAQUS

Figure 1: Comparison of Prototype and ABAQUS Model

In order to achieve realistic simulations, assumptions were made based on previous literature on the interactions and connections between structural components to ensure that these assumptions accurately reflect the mechanical relationships and constraints found in real buildings.

Primary and secondary structural members were modeled using real-world contours and dimensions that reflect the typical design of metal building systems. Wind loads from tornadoes were modeled using data measured from the Texas Tech University Tornado Simulator on a scaled model of the building. By combining high-fidelity numerical modeling with experimentally verified loading conditions, this study provides a comprehensive analysis of the buckling capacity and overall performance of the roof system in metal buildings under tornado-induced dynamic loading and compares it with static analyses.

2. Laboratory measurement of tornado loading

The experiment was conducted in the tornado simulator at Texas Tech University. A tornado-like vortex, as Fig. 2a shown, can be generated within the facility. The core radius r_c of a generated tornado-like vortex, which is defined as the radial distance where the maximum tangential velocity is observed, is 0.87 m. In this study, a 1:200 scaled metal building model as Fig. 2c shown was tested in the tornado-like vortex to measure the tornado induced pressure on the model. Fig. 2b shows schematics of a typical configuration of laboratory testing. The length, width, height and roof slop of building model is 190 mm, 123 mm, 30 mm, and 1/24 respectively. The building

model has 216 external pressure taps and 3 internal pressure taps with 625 Hz sampling rate, and the layout of those taps is shown in Fig. 2d. In addition, the building model has 72 holes to simulate small leaks of a real building, and the leakage ratio, defined as area of leakages over area of building envelope, is 0.2%. All the pressures are represented by pressure coefficients as shown in Eq. 1:

$$C_p = \frac{P - P_{ref}}{0.5\rho\left(\overline{V}_{\theta,\max}\right)^2} \tag{1}$$

where C_p is the pressure coefficient, P_{ref} is the static pressure beneath the moving floor, ρ is the air density, which is 0.075 lb/ft^3, and $\overline{V}_{\theta,\max}$ is the maximum mean tangential velocity, which is 28 mph.

This study examined two scenarios to model the interaction between a metal building and tornadoes. In the first scenario, the tornado is stationary, and the building model is positioned at $x/r_c = -0.5, y/r_c = 0$ with the building orientation β at 0 degrees. The sampling duration for this scenario is 120 seconds. Fig. 3a presents the time history of pressure coefficients induced by the stationary tornado for an internal tap and an external tap located at the center of the roof. Fig. 3b provides a contour plot of the instantaneous net pressure coefficient at 60 seconds. These figures suggest that the net pressure coefficient can be significantly reduced due to the equilibrium between external and internal pressures.

In the second scenario, the tornado translated through the center of the building model at a speed of 0.25 m/s. Due to the non-stationary loading that a moving tornado imposes on buildings, the test was repeated 100 times to reduce uncertainty of tornado loading. Fig. 4a illustrates one realization of the position-varying pressure coefficient for an external tap at the center of the roof and an internal tap as affected by the moving tornado, with the relative distance between the tornado's center and the building normalized by core radius r_c. Fig. 4b shows a contour plot of the instantaneous net pressure coefficient when the building model is at $x/r_c = -0.5$. The figure clearly indicates that the top left corner of the building model experiences high suction pressure.

(a)

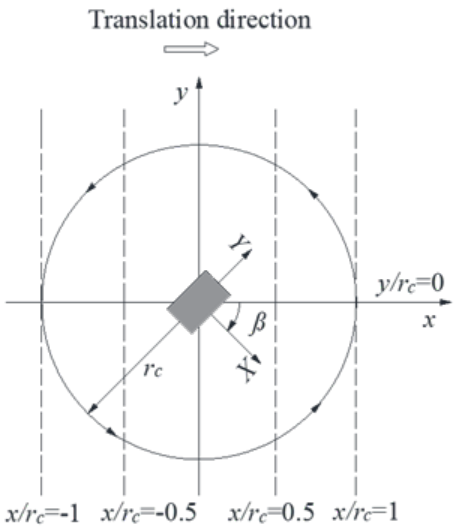

(b)

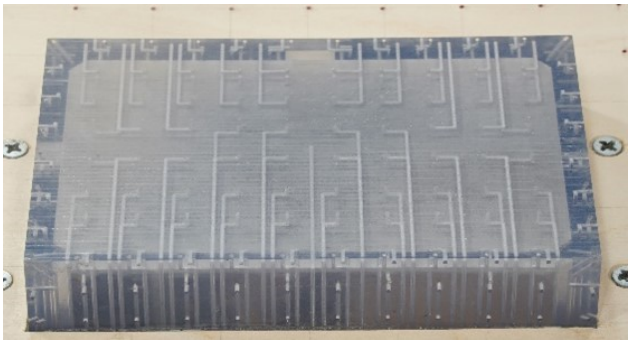

(c)

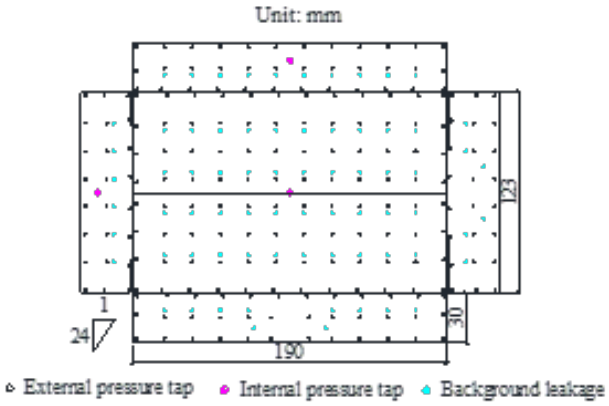

(d)

Figure 2: Tornado simulator and model: (a) A photo of generated tornado-like vortex; (b) Schematics of a typical test configuration with a global coordinate system and a local coordinate system; (c) A photo of tested building model; (d) Layout of the pressure taps and distributed leakages on the building model.

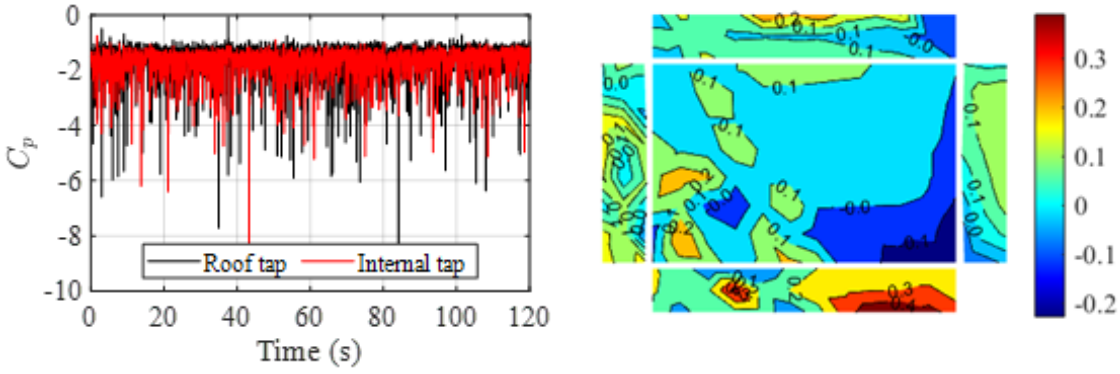

(a) (b)

Figure 3: (a) Time history of the pressure coefficient for a external tap at center of roof and a internal tap subjected to a stationary tornado; (b) Contour plot of instantaneous net pressure coefficient at 60 seconds.

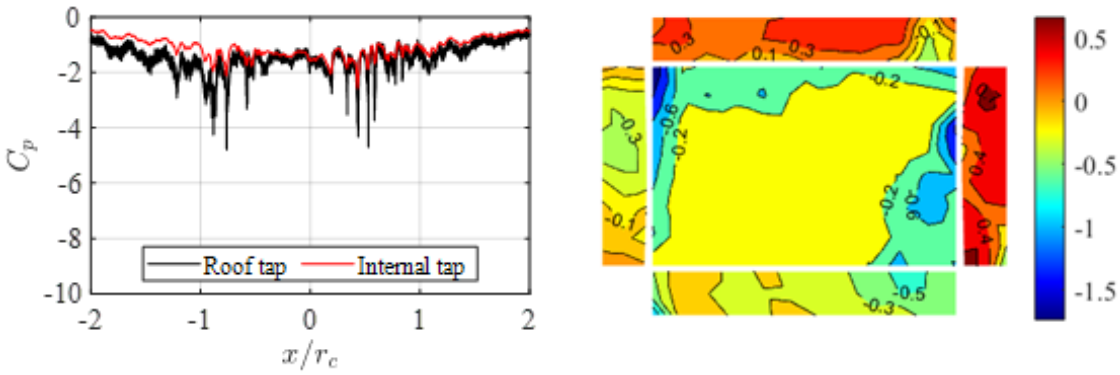

(a) (b)

Figure 4: (a) Position varying pressure coefficient for a external tap at center of roof and a internal tap subjected to a moving tornado; (b) Contour plot of instantaneous net pressure coefficient when building model is at $x/r_c = -0.5$.

3. Finite Element Modeling on a Roof Section

To accurately capture the behavior of the roof panels, two detailed submodels of the roof (shown in Fig. 5) were created, which includes key structural components such as rafters, flange bracing, eaves, purlins, and cleats. The roof submodel represents one bay span (from center to center of a bay) and from one the eave to apex on one side, for a total size of 26 ft by 39 ft. The difference between the two models is the presence of the sag angle. Occasionally, a contractor may forget to include the sag angles, and the impact of the sag angle is investigated in this paper.

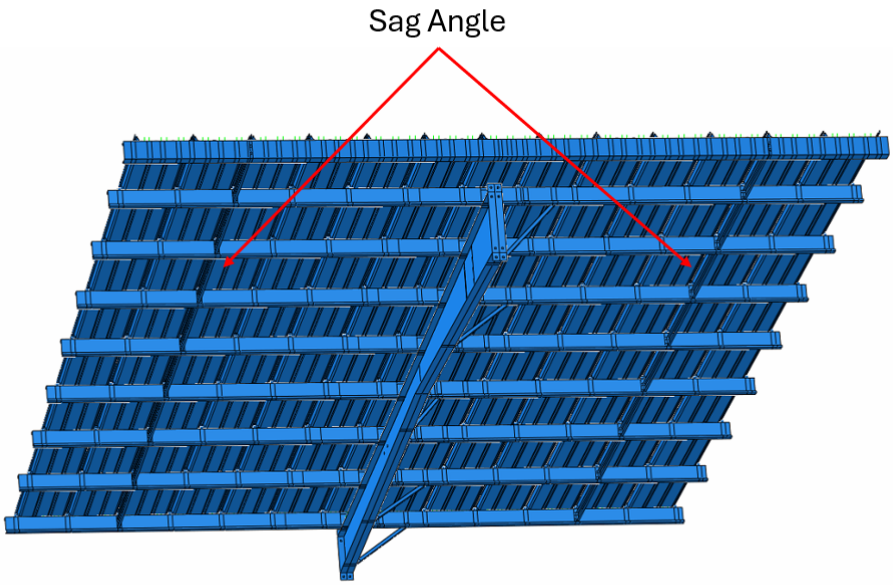

Figure 5: submodel of the roof panel

3.1 Material Property and Parts Detail

Based on previous literature, the components are represented by S4R shell elements (Yu and Schafer, 2006; Bajwa, 2010; Hong, 2007; Niari, Rafezy, and Abedi, 2015; Kim, 2010).

To account for the sensitivity of the member response to yielding and post-yield behavior, detailed material models for both hot-rolled steel (HRS) and cold-formed steel (CFS) were included in the finite element analyzes. Previous studies by Sadowski et al. (2015) and Young et al. (1999) have found significant differences in the nonlinear post-yield behavior of HRS and CFS. In this study, the material modeling of the HRS cross section was adopted from Yun et al. (2017), while the model for the CFS sections is derived from Gardner et al. (2018). These two references integrate and analyze a large amount of test data from a variety of published experiments to create a representative material model that requires only the input of the yield stress to generate a complete stress-strain curve.

All components in the submodel were made of CFS except for the rafters fabricated from HRS. The yield stress of the cold-formed section was 55 ksi and the modulus of elasticity was 29,500 ksi, and the yield stress of the HRS was 50 ksi and the modulus of elasticity was 29,000 ksi. Both steels had Poisson ratios of 0.3 and densities of 0.284 lb/in^3. All stress-strain data were converted to true stress and true strain for accurate implementation in ABAQUS. The corresponding thicknesses for each type of elements are provided in Table 1. In addition, the middle portion of the purlin around the cleat area was modeled with double thickness to account for purlin overlap in actual construction.

Table 1: Material and thickness on parts

Part name	Material	Thickness (in)
Rafter-Flange	HRS	0.375
Rafter-Web(Column side)	HRS	0.156
Rafter-Web(Rafter side)	HRS	0.125
Rafter-Splice(Column side)	HRS	0.75
Rafter-Splice(Rafter side)	HRS	0.5
Flange Bracing	CFS	0.125
Eave	CFS	0.1
Cleat	CFS	0.19
Purlin	CFS	0.075
Roof panel	CFS	0.03
Sag angle	HRS	0.125

3.2 Boundary conditions

The bolt connections between the flange supports and the rafters are modeled using MPC beam constraints, following the method established by Moen et al. (2019). This method transfers rotations and displacements to the corresponding coupling regions. In addition, the bolt connections between the cleats, rafter upper flanges, sag angle and purlins were modeled using tie constraints to ensure proper interaction.

The connections between eave and column and between column and rafter were simplified by constraining all degrees of freedom, which follows the methodology established by Moen et al. (2019). Since this model represents a middle-bay-to-middle-bay half-frame submodel, appropriate symmetry boundary conditions were applied in the cutting planes. These boundary conditions include limiting movement towards the plane of symmetry and limiting rotation around the other two axes in order to accurately represent the structural behavior in the simulation. The connection between the eaves and the purlins at the ridge was modeled using rigid MPC fasteners. The clips connecting the roof panels to the purlins (Fig. 7) were represented as connectors with a slotted cross-section (Fig. 6). Although this approach is similar to the one proposed by Darwish and ElGawady (2023), the connectors do not have equivalent stiffness. Instead, the cross-section of the slot allows sliding entirely in the panel direction while limiting displacement along the other axes. Sliding displacement along the panel direction is limited to 1.25 inches, and a slight stiffness is incorporated into the connector to account for frictional effects.

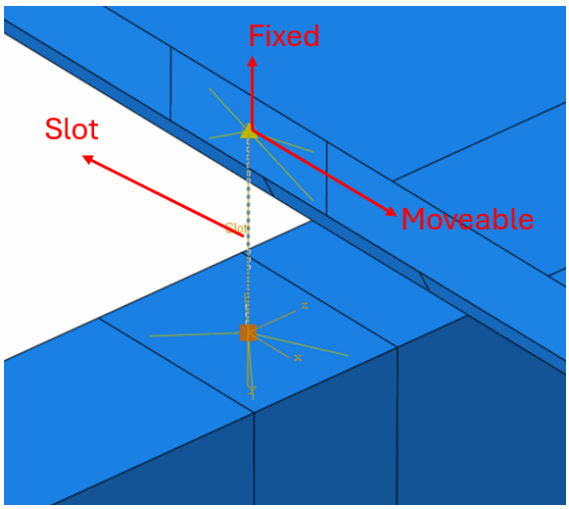

Figure 6: Clip modeled as slot

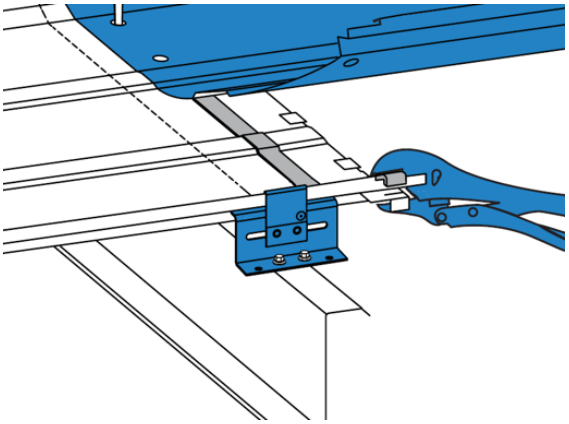

Figure 7: Clip drawing

3.3 Part simplification

The roof panels cross section was imported from a 2D CAD file and had to be simplified (Fig. 8) in the model to address meshing challenges, in particular to avoid high aspect ratios (Fig. 9) of the mesh elements. The specific reason for this is that the original design on both sides of the center protrusion of the panel has several very long and thin sections, and the width in the thin sections is too small in proportion to the original mesh of the panels on the outside. It is worth noting that the flat portion of the roof panel can sometimes become uneven from side to side when imported into ABAQUS. Even though there is only a fraction of a foot difference per panel, with such a large building, it can lead to significant unevenness in the front portion of the wall or roof. The mesh size for the other parts of the roof submodel will be discussed in Sections 4.1.1 and 4.2.1.

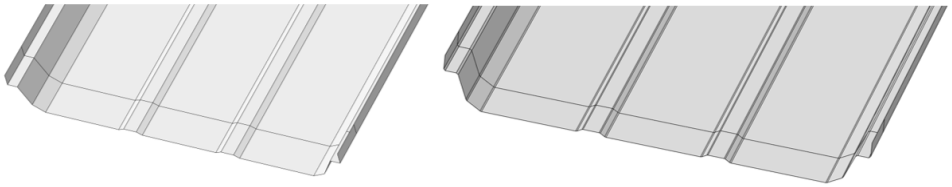

Figure 8: Simplified roof (left), Regular roof panel (right)

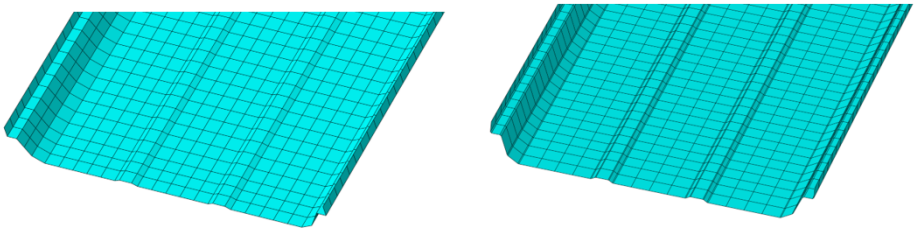

Figure 9: Simplified roof mesh (left), Regular roof panel mesh (right)

4. Analysis

In this paper, static and dynamic explicit analyses are used to simulate the structural behavior of a metal building roof submodel under different loading conditions. The static analysis, which assumes the application of static loads, is compared with the dynamic explicit analysis that incorporates load fluctuations over time and inertial effects. Furthermore, under each type of analysis, the structural response is evaluated for three distinct loading scenarios: (1) a uniform load to quantify differences between static and dynamic analyses, (2) the moving tornado load, and (3) the stationary tornado load to represent tornado conditions.

4.1 Dynamic Analysis

4.1.1 Mesh

The entire building was modeled using the S4R explicit default element types from the ABAQUS element library. Since the minimum step time depends on the shortest edge of the smallest element and there is no convergence problem in dynamic analysis, the mesh size can be relatively large but should be small enough to capture the local buckling. The mesh size is shown in Table 2.

Table 2: Mesh size in dynamic analysis

Part name	Mesh Size (in^2)
Rafter	1.5
Flange Bracing	0.5
Eave	1.4
Cleat	1
Purlin	1.4
Roof panel	1
Sag angle	1.4

4.1.2 Tornado load applied

Before apply loading to FEA model, it is necessary to convert the laboratory measured tornado loading to realistic tornado loading pressure (p) on the building according to Eq. 2:

$$p = C_{p\_net} \times 0.5\rho \left(V_{ref}\right)^2 \tag{2}$$

where $C_{p,\text{net}}$ is the net pressure coefficient for each tap, V_{ref} is the maximum mean tangential velocity of a tornado, and ρ is the air density, which is 0.075 lb/ft^3.

The load cases in this submodel were extracted from the distribution of pressure coefficients at the middle frames of the entire roof panel. The total length of the 40-foot panels was divided into four equal sections, while the 13 roof panels were divided into three zones with widths of 3, 7, and 3 panels, respectively. Each section was assigned a corresponding time-dependent loading coefficient.

4.1.3 Step setup

The total simulation time was 174.8 seconds, representing the entire duration of the tornado's impact on the metal building system. To optimize computational efficiency, mass scaling was used to reduce the overall computational time. The rule is that the process is considered quasi-static if the kinetic energy does not exceed 5-10% of the internal energy throughout the simulation. Under these conditions, the response of the model is not significantly affected by acceleration effects, which means that mass scaling reflected in the adjusted material density does not affect the results.

4.2 Static Analysis

4.2.1 Mesh

Unlike the dynamic analysis, the static analysis is more sensitive to convergence issues and therefore requires more attention to the mesh arrangement.

In this study, the mesh seed density of critical areas such as purlin upper flange, purlin web, cleat and vertical region of roof panel is two times of the conventional mesh seed density of the same section. The mesh size is shown in Table 3.

Table 3: Mesh size in static analysis

Part name	Mesh Size (in^2)
Rafter	0.5
Flange Bracing	0.3
Eave	0.25
Cleat	0.5
Purlin	0.5
Roof panel	0.5
Sag angle	0.15

4.2.2 Tornado load applied

In the static analysis under tornado loading, the load application methodology extracts the time at which the peak pressure occurs in the tornado loading experimental dataset and applies the pressure at that time to each area, corresponding to the related pressure tap, of the panel across the entire roof slab. The static analysis then incrementally applies increasing load up to that pressure.

4.2.3 Step setup

The nonlinear geometry option is enabled during the static analysis to ensure that large deformations and rotations are accounted for in the simulation. The analysis type is general static.

5. Result

5.1 Comparison of Static and Dynamic Results on Uniform Load

A comparative assessment of the structural response under uniform roof lifting loads of 0.2 psi and 0.3 psi was performed using two analytical methods in ABAQUS, static and dynamic explicit, both with and without the sag angle. It is important to clarify that these uniform loads differ significantly from the previously discussed tornado-related loadings. The simple uniform load cases presented here represent constant, non-varying pressure applied evenly across the entire roof surface, allowing for a straightforward comparison of the static and dynamic analytical results. Eight simulations (Job-1 to Job-8) were analyzed and are described in Table 4.

Table 4: Analysis job details for uniform applied load

Part name	Analysis type	Load magnitude	Sag angle
Job-1	Static	-0.2psi	N
Job-2	Static	-0.3psi	N
Job-3	Dynamic	-0.2psi	N
Job-4	Dynamic	-0.3psi	N
Job-5	Static	-0.2psi	Y
Job-6	Static	-0.3psi	Y
Job-7	Dynamic	-0.2psi	Y
Job-8	Dynamic	-0.3psi	Y

In Job-1, the total strain energy amounted to 46,713.8 in-lbf with a corresponding total vertical reaction force of -29,290 lbs. In Job-2, the total strain energy increases to 91,309.7 in-lbf, while

the sum of the vertical reaction forces is -43,920 lbs.

To match the energy state of the static models, specific time increments were selected in the dynamic explicit models. For Job-3, corresponding to the 0.2 psi load, a time increment within a certain loading step was identified. At this point, the strain energy was 46,837.9 in-lbf, reflecting a discrepancy of less than 1% from the Job-1 static model, demonstrating comparable energy absorption characteristics. However, the total reaction force at this stage was -26,406 lbs, representing a 10% reduction relative to the static result. The maximum difference in stress between Job-1 and Job-3 is obtained by the ratio $^{58,680}/_{62,230} = 0.943$, corresponding to a 5.7% variation. For displacement, the maximum difference is given by $^{6.459}/_{5.596} = 1.155$, representing a 15.5% variation.

For Job-4, corresponding to the 0.3 psi load, a time increment within a certain loading step was selected. Here, the strain energy was 90,918.6 in-lbf, also within 1% of the static reference, confirming consistency in global energy absorption across the two analysis approaches. The total reaction force was -45,331 lbs, representing a smaller 3.2% reduction relative to the static model. The maximum stress difference between Job-2 and Job-4 is given by $^{77,331}/_{71,220} = 1.086$, which corresponds to an 8.6% difference. Similarly, the maximum displacement difference is given by $^{9.373}/_{11.81} = 0.794$, representing a 20.6% difference.

In Job-5, the total strain energy amounted to 47937.5 in-lbf with a corresponding total vertical reaction force of -27521.9 lbs. In Job-6, the total strain energy increases to 93027.4 in-lbf, while the sum of the vertical reaction forces is -42392.7 lbs. The corresponding step in Job-7, which has a similar strain energy of 45,926.3 in-lbf, has a total vertical reaction of -24,151.8 lbs. Job-8 has a total vertical reaction of -38,831.7 lbs, while the strain energy is 91,134.6 in-lbf. The reaction difference between Job-5 and Job-7 is 14%, while the energy difference is 4%. The reaction difference between Job-6 and Job-8 is 9%, while the energy difference is 2%. The maximum stress and maximum displacement differences between Job-5 and Job-7, and Job-6 and Job-8, are 54%, 31%, 14%, and 50%, respectively.

5.2 Comparison of Static and Dynamic Results under Moving Tornado Load

The buckling behaviors were captured in four analyses, differing by the presence or absence of the sag angle and the analysis type (static or dynamic). The reference wind speed is selected at 156 mph based on the experiment result observed in the moving tornado test. The wind pressure is much higher and concentrated at the corner, while the middle span does not receive enough pressure to fail the roof in that location. In order to capture the buckling behavior, a rather high value was selected to make the peak pressure in the middle span the same as the corner peak pressure under 111 mph, which is selected for stationary tornado. These four simulations (Job-9 to Job-12) are described in Table 5.

Table 5: Analysis job details for pressure due to moving tornado

Part name	Analysis type	Reference wind speed	Sag angle
Job-9	Dynamic	156 mph	N
Job-10	Dynamic	156 mph	Y
Job-11	Static	156 mph	N
Job-12	Static	156 mph	Y

5.2.1 Dynamic analysis

For Job-9, the energy ratios of internal energy to kinetic energy were calculated to be ${}^{6612.93}/_{88981.8} = 0.07$ for the entire model and ${}^{4015.12}/_{77557.8} = 0.05$ for the roof panel only. Both ratios are within the acceptable range of 5% to 10%, ensuring that the kinetic energy is kept low enough in relation to the internal energy while at the same time ensuring that the results are consistent with the quasi-static behavior of the system.

The captured buckling behaviors include local buckling in the roof panel (Fig.10), local buckling in the clip area (Fig.11), and distortional buckling in the purlin (Fig.12). However, local buckling in the flanges and webs of the purlin was not observed with the absence of a sag angle.

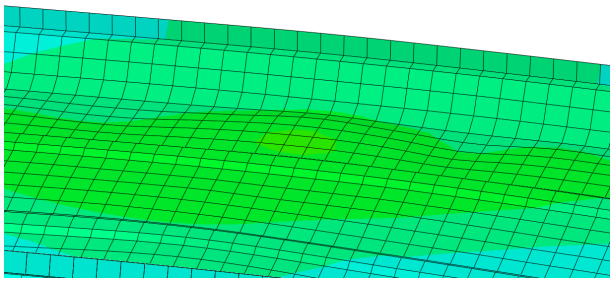

Figure 10: Local buckling on the roof panel

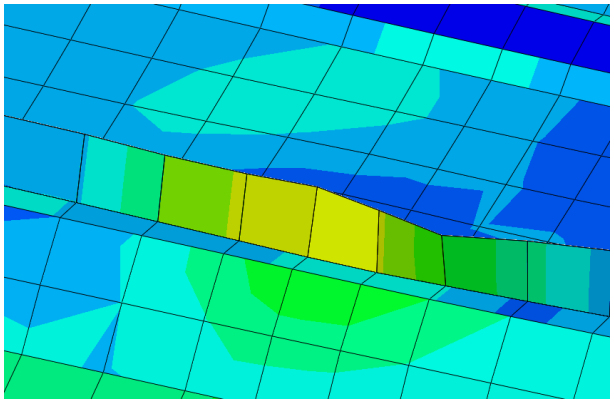

Figure 11: Local buckling on the clip area

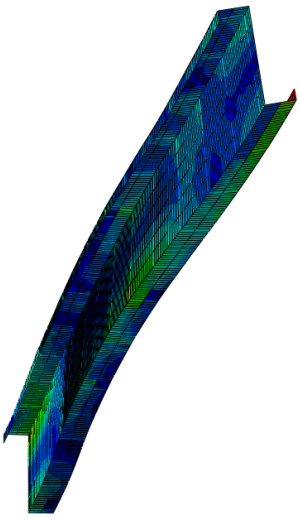

Figure 12: Distortional buckling on purlin

For Job-10, the energy ratio of internal energy to kinetic energy was calculated to be 0.013, which is significantly lower than 5%. The captured buckling behaviors include local buckling in the roof panel and around the clip area (Fig.13), and local buckling on the sag angle (Fig.14).

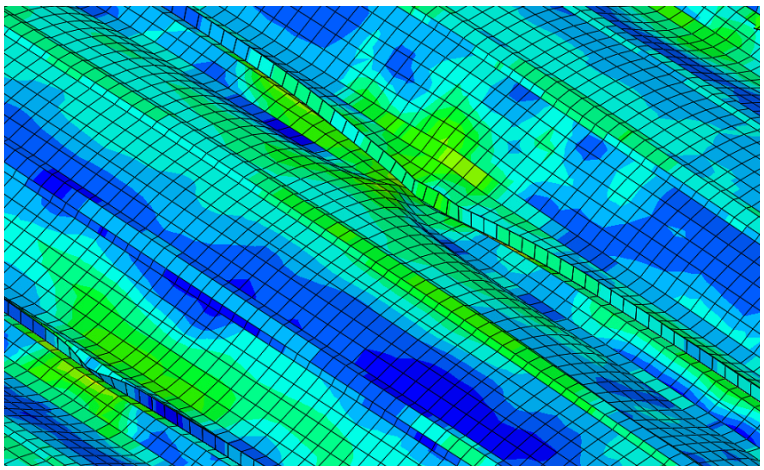

Figure 13: Local buckling on the roof panel and clip area

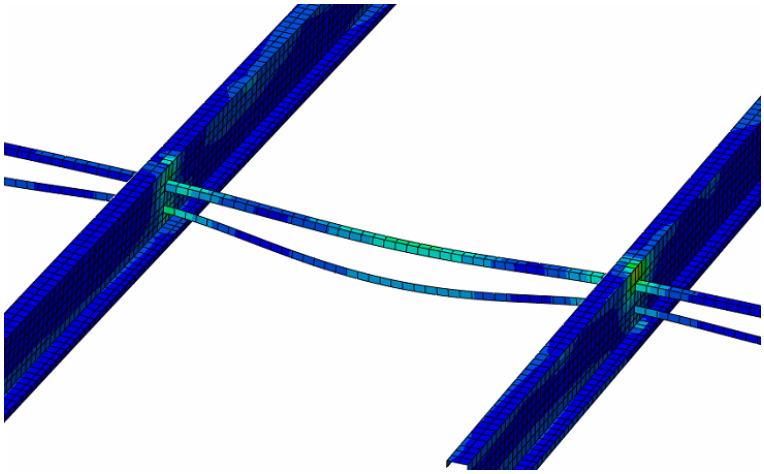

Figure 14: Local buckling on the sag angle

5.2.2 Static analysis

No buckling was observed in the roof panel in Job-11, while distortional buckling was identified in the purlin (Fig.15).

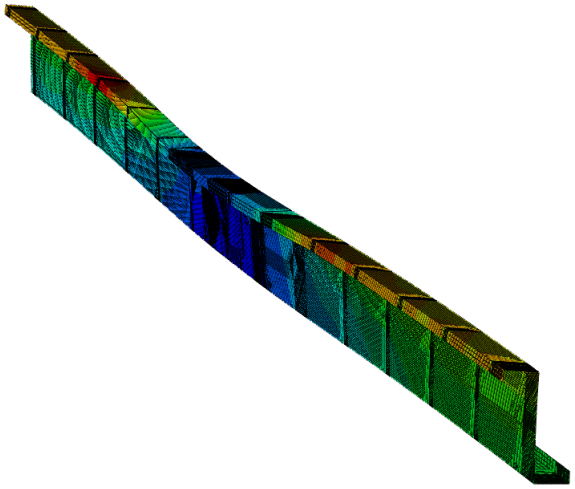

Figure 15: Distortional buckling on purlin

In Job-12, no buckling was observed.

5.3 Comparison of Dynamic Results under stationary tornado load

Two simulations, Job-13 and Job-14, are described in Table 6. The energy ratio of internal energy to kinetic energy was calculated to be around 1%, indicating that they are quasi-static analyses.

Table 6: Analysis job details for stationary tornado load

Part name	Analysis type	Reference wind speed	Sag angle
Job-13	Dynamic	111 mph	Y
Job-14	Dynamic	111 mph	N

For Job-13, the captured buckling behaviors include local buckling in the roof panel and around the clip area (Fig.16), and local buckling on the sag angle (Fig.17).

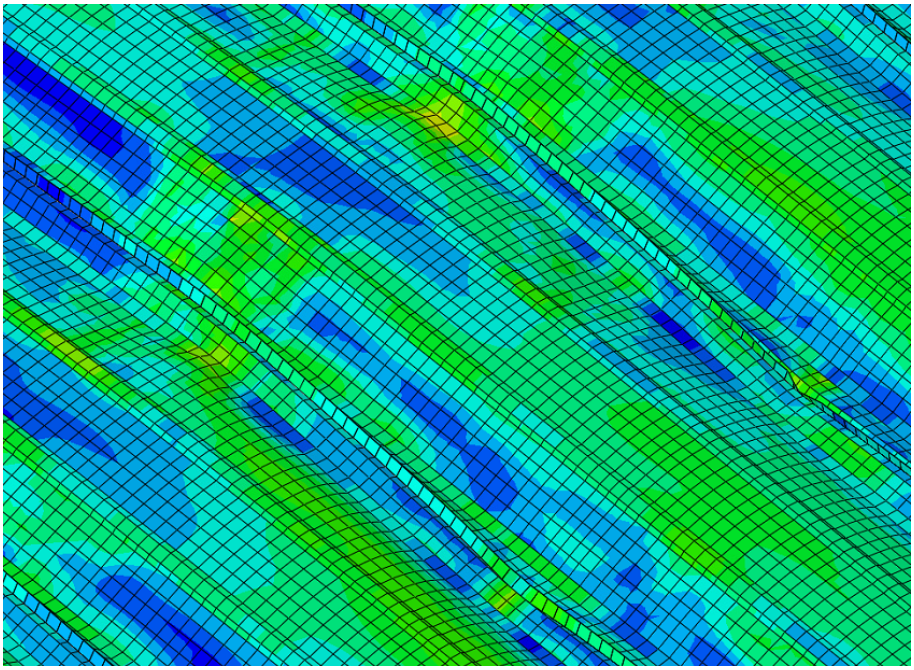

Figure 16: Local buckling on the roof panel and clip area

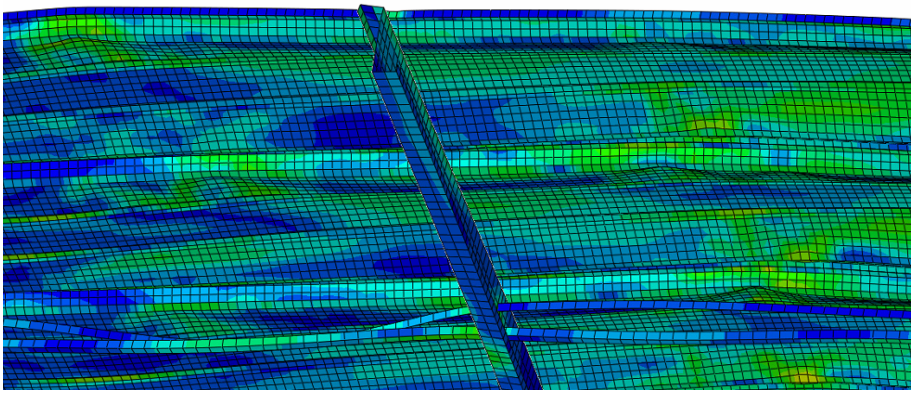

Figure 17: Local buckling on the sag angle

For Job-14, the captured buckling behaviors include local buckling in the roof panel and around the clip area (Fig.18). Distortional buckling and local buckling was observed in the purlin (Fig.19).

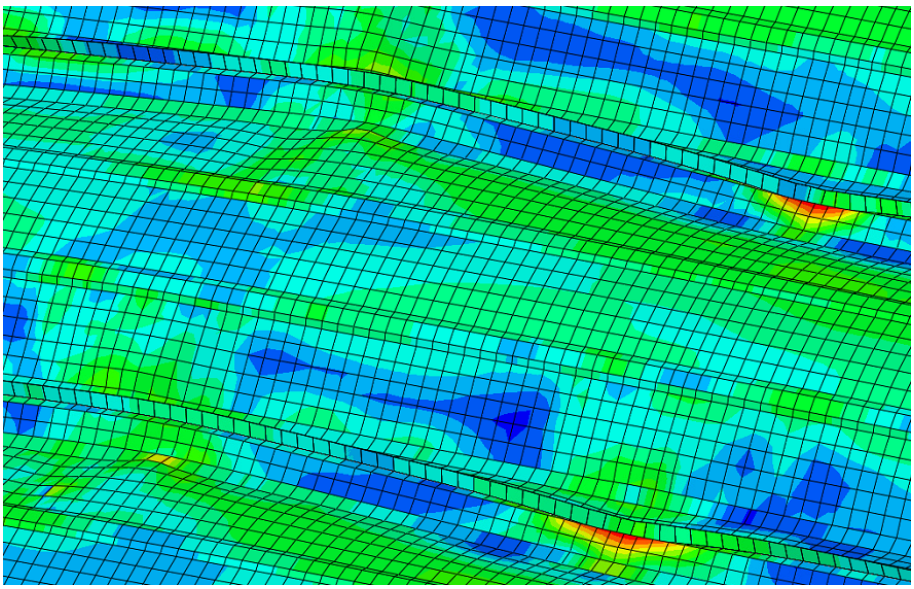

Figure 18: Local buckling on the roof panel and clip area

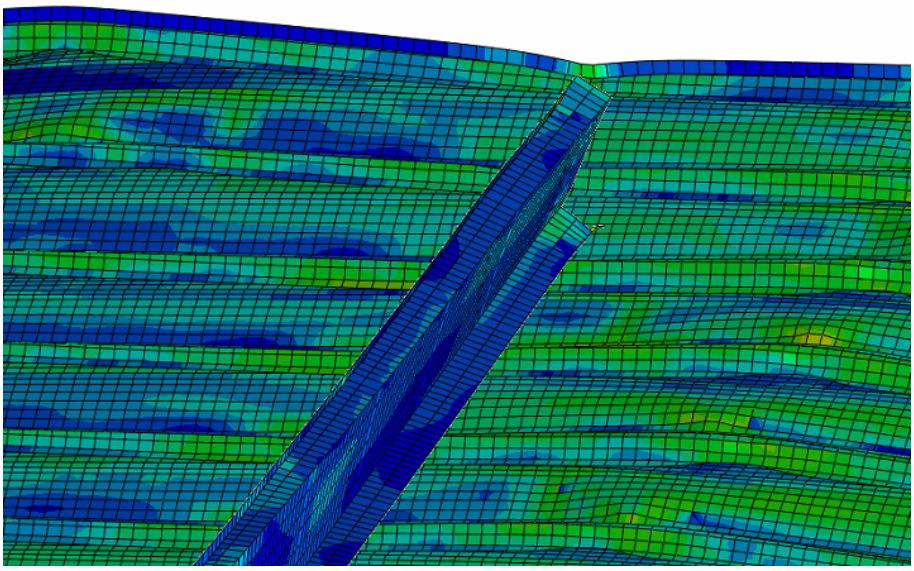

Figure 19: Distortional and local buckling in purlin

6. Discussion

6.1 Discussion on the Comparison of Static and Dynamic Results on Uniform Load

The results show that both static and dynamic explicit analyses have similar overall structural responses when evaluated at equivalent strain energy levels. The matching magnitude of reaction forces at the point of matching strain energy indicates that the dynamic model has reached a loading state close to the static equilibrium state.

However, when the strain energies match, there are also differences in stresses and displacements.

These differences can be caused by the differences between the underlying solution methods. Unlike the static method, the dynamic explicit method incorporated inertial effects and accounts for loading velocities, which could result in differences in stress distribution and displacement response. This difference increases with higher loading levels, indicating that nonlinear effects and local stress concentrations become more pronounced.

Despite the differences in stresses and displacements, the similarity in the shapes of the reaction forces and the overall stress distribution can indicate that the overall deformation pattern produced by the two methods is the same. Also from an energy perspective, this agreement indicates that the two analyses reflect similar stiffness behavior and deformation mechanisms, suggesting that the dynamic explicit solution is effective in capturing the underlying structural behavior under load.

6.2 Discussion on the results of Static and Dynamic Results under Moving Tornado Load

Dynamic and static analyses showed significant differences in buckling behavior and structural response. In dynamic analyses, local buckling in the clip areas and roof panels and torsional buckling on purlins were found. In contrast, the static analysis with peak loading applied showed torsional buckling only in the purlins, and no local buckling in any components. Additionally, the dynamic analysis showed higher stresses but smaller displacements compared to the static analysis.

Since under the dynamic conditions the load is temporal, continual changing of the load could lead to frequent stress redistribution. The local instability would be triggered on the thin components like clip areas and roof panels. It would also lead to higher stress differences in certain areas. However, under static loading, stress redistribution is more uniform throughout the structure, which reduces the likelihood of local buckling, leading to lower stress intensities but larger cumulative deformations.

In both analyses, the purlins did not show local buckling, suggesting that the absence of sag angles may be responsible. The purlins had a long unsupported effective length and lacked the necessary lateral restraint. As the results show, the slender profile makes it more susceptible to torsional buckling under both dynamic and static loading conditions.

6.3 Comparison of Dynamic Results under Stationary Tornado Load

Both analyses show local buckling on the roof panel and around the clip area. In contrast, the presence of the sag angle prevents the purlin from rotating and mitigates torsional and local buckling. The model without the sag angle exhibits both types of buckling on the purlin.

7. Future work

In future work, a detailed submodel of roof corners will be developed. More detailed structural components on the side rafter that interact with the end walls will be incorporated into the submodel.

In metal buildings subjected to tornado, failure may occur at the connections and therefore modeling realistic connection behavior is important. Therefore, rigid connections in the current model should be replaced with connectors with appropriate stiffness.

8. Conclusions

In this study, detailed finite element models of a portion of a metal building roof, with and without sag angles, were developed using ABAQUS to investigate their structural behavior under tornado wind loads. The model has realistic geometry and nonlinear material properties, with some assumptions on the boundary conditions and connections. These submodels were subjected to various wind load scenarios, including uniform loads to compare differences between dynamic and static analyses, and dynamic and stationary tornado loads to represent the actual tornado loading. The results from the static and dynamic explicit analyses were compared including reaction forces, stress distributions, displacement patterns, and the failure mode on the metal building roof system.

The reaction forces at the support boundaries remain consistent under uniform lift loads of 0.2 psi and 0.3 psi under the same energy level, indicating that the dynamic analysis in this study can achieve a state similar to static analysis. When the structure was subjected to a moving tornado load, distinct differences in buckling behavior and stress distribution emerged between the static and dynamic simulations. The dynamic analysis had more complex local buckling behavior, including local buckling on clips area and roof panels, as well as distortional buckling on the purlins. In contrast, the static analysis identified distortional buckling in the purlins only, without indicating any local buckling in other components.

Notably, when comparing the results under both moving and stationary tornado load with the sag angle in the model, buckling on the purlins was prevented as the sag angle resulted in a shorter purlin unbraced length. Sag angles influenced the buckling shape of the roof panel, and caused stress to concentrate around the clips. This lead to higher displacement and buckling in the connection area, indicating the importance of accurate connection modeling.

References

Abaqus (2016). *version 6.16*. Dassault Systèmes Simulia Corp.

Bajwa, Maninder Singh (2010). "Assessment of Analytical Procedures for designing metal buildings for Wind drift serviceability". PhD thesis. Virginia Tech.

Darwish, Yasser and Mohamed ElGawady (2023). "Finite element analysis of TPO membrane-retrofitted metal roof system subjected to wind loads". *Structures*. Vol. 50. Elsevier, pp. 330–346.

Federal Emergency Management Agency (FEMA) (1999). *Building Performance Assessment: Oklahoma and Kansas Tornadoes*. Technical Report. Washington, D.C.: Federal Emergency Management Agency (FEMA).

Gardner, Leroy and Xiang Yun (Nov. 2018). "Description of stress-strain curves for cold-formed steels". *Construction and Building Materials* 189, pp. 527–538. ISSN: 09500618. DOI: 10.1016/j.conbuildmat.2018.08.195.

Hong, Jong-Kook (2007). *Development of a seismic design procedure for metal building systems*. University of California, San Diego.

Kim, Yoon Duk (2010). *Behavior and design of metal building frames using general prismatic and web-tapered steel I-section members*. Georgia Institute of Technology.

Moen, Cristopher D, Shahab Torabian, and Benjamin W Schafer (2019). *Evaluation of Metal Building System Seismic Response Modification Coefficients*. Tech. rep.

Niari, Shirin Esmaeili, Behzad Rafezy, and Karim Abedi (2015). "Seismic behavior of steel sheathed cold-formed steel shear wall: experimental investigation and numerical modeling". *Thin-Walled Structures* 96, pp. 337–347.

Rogers, Colin A. and Robert Tremblay (2010). "Impact of diaphragm behavior on the seismic design of low-rise steel buildings". *Engineering Journal* 47 (1). ISSN: 00138029. DOI: 10.62913/engj.v47i1.974.

Sadowski, Adam J. et al. (2015). "Statistical analysis of the material properties of selected structural carbon steels". *Structural Safety* 53. ISSN: 01674730. DOI: 10.1016/j.strusafe.2014.12.002.

Telue, Yaip and Mahen Mahendran (2004). "Numerical modelling and design of unlined cold-formed steel wall frames". *Journal of Constructional Steel Research* 60.8, pp. 1241–1256.

Young, Ben and Kim J.R. Rasmussen (1999). "Behaviour of cold-formed singly symmetric columns". *Thin-Walled Structures* 33 (2). ISSN: 02638231. DOI: 10.1016/s0263-8231(98)00044-5.

Yu, Cheng and Benjamin W Schafer (2006). "Finite element modeling of cold-formed steel beams validation and application".

Yun, Xiang and Leroy Gardner (June 2017). "Stress-strain curves for hot-rolled steels". *Journal of Constructional Steel Research* 133, pp. 36–46. ISSN: 0143974X. DOI: 10.1016/j.jcsr.2017.01.024.